

Engineering Design Review

Legendary Rover Team

May 5, 2021



LEGENDARY
RZESZOW UNIVERSITY OF TECHNOLOGY



Team Project Lead Name: Hubert Gross
E-mail: team.legendaryrover@gmail.com

1 Orthographic/Isometric Image of UAV

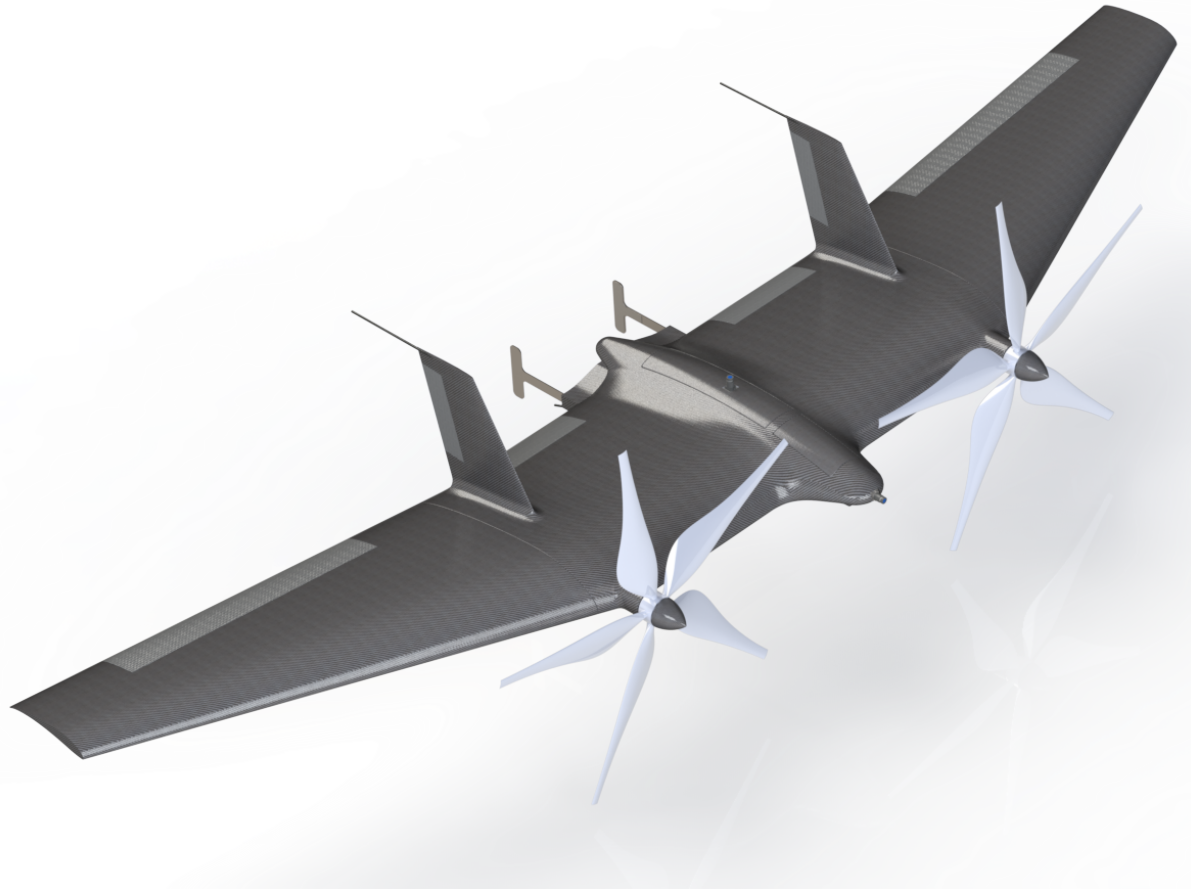


Figure 1: Isometric Image of the Falcon

- Propellers - airfoil designed for maximum lift forces
- Wings - based on PICA and Buckypaper materials, extremely light and robust
- Fuselage - contains all the electronics and science devices
- Package Picking Mechanism - fast, robust, easily lifts packages up to 30cm wide
- Science Package System - sampling through an inlet on the fuselage nose
- Vision - 3 cameras (on nose, top and bottom) provides 360° vision
- Ion Turbulizers - significant improvement of the aerodynamic characteristics of the airfoil

2 Mars Environment Analysis

This section covers concise and compact Martian environment and eventual circumstances summary, related to conditions on which the target vehicle should be operated.

2.1 Atmosphere Analysis

The atmosphere of Mars and the conditions on Mars are significantly different from those of Earth. Chemical composition, wind speed, pressure, gravity, temperatures, dust and topography are significantly different. This influences UAV mobility, aerodynamics (rudder efficiency, wing and propeller profiles, UAV geometry, Reynolds number, wind gusts), physical parameters (drag forces, lift force), electronics (extreme temperatures, radiation), equipment operation (fine dust, difficult to analyze terrain topography) and many others.

Atmosphere

The atmospheric composition varies according to the sources cited, which is due to the type of measurement (electronic sensors, spectrometers) and the measurement location. However, these differences are of the tenths of a percent at most. Scientists are still looking for possible processes and chemical reactions responsible for the formation of chemical compounds, and the origin of some is unknown (e.g. methane) [1, 2].

Gas name	Chemical symbol	Amount
Carbon Dioxide	CO_2	95,1%
Nitrogen	N_2	2,59%
Argon	Ar	1,94%
Oxygen	O_2	0,16%
Carbon Monoxide	CO	0,06%
Water	H_2O	210ppm
Nitrogen Oxide	NO	100ppm
Neon	Ne	2,5ppm
Hydrogen-Deuterium-Oxygen	HDO	0,85ppm
Krypton	Kr	0,3ppm
Xenon	Xe	0,08ppm

Table 1: Chemical composition of Mars atmosphere in percent or ppm[3]

Gravity acceleration

The gravity acceleration on Mars varies depending on the topography of the terrain and the distance from the surface. In the case of UAV flying on Mars at low altitudes (less than 500m), mean surface gravity acceleration can be used for calculations. According to Mars Gravity Model 2011 (MGM2011) it is $3.72076 \frac{m}{s^2}$ [4].

Others

Temperatures on Mars range from -153° at the poles, all the way up to 30° . At night the air is saturated (100% humidity), but during the day is undersaturated. Wind on Mars can be about $30m/s$ and create dust storms that take months to settle. All of that information significantly changes the approach to UAV flight. Deciding when to launch

and when it will be too risky is crucial to ensure that the Falcon will be safe and fulfill its tasks [5, 6].

2.2 Mars Atmosphere Model

Designing a UAV operating on martian atmospheric condition requires a comprehensive martian atmospheric conditions analysis. The Mars Atmosphere model [7] was originally derived from the Standard Atmosphere model [8] adapted to the martian atmospheric conditions. For the purposes of aerodynamic calculations it is assumed simplifying that the martian atmosphere consists only of However, [7] does not define a kinematic viscosity required in order to evaluate the Reynolds numbers that appear on different sections of aerodynamic surfaces. According to this fact, a rough values of Dynamic Viscosity $\mu = 6.65 \cdot 10^{-4}$ and local fluid density $\rho = 0.017 \frac{kg}{m^3}$ were assumed, according to [9]. Having these fundamental fluid parameters defined, a rough estimates of local Reynolds numbers from now onward may be determined.

Yet [7] is still could useful while describing the atmospheric parameters related to UAV's operating ceiling. The considered UAV **is not expected to operate** at altitudes higher than *500 meters*, giving lower density limit equal to $\rho_{min} \approx 14.4 \cdot 10^{-3} \frac{kg}{m^3}$.

3 UAV Structure

3.1 Overview

Proposed UAV structure belongs to a tailless-type aeronautical arrangement. The UAV's propulsion consists of two five-bladed counter-rotating propellers each powered by a single brushless electrical motor. The detailed description of the power plant could be found in Section 5 of this document.

The innovative and outstanding feature of the proposed arrangement is its VTOL capabilities - it is assumed that the aircraft takes off from vertically-situated orientation; then, according to current flight stage demands, it could stay in vertical, "hovering" orientation, or translate to a horizontal orientation, converting itself to a airplane. The center wing section is self-sustainable drone with a possibility of separation the wingtip sections, leaving the most of the control surfaces necessary for the flight control in hovering mode. This particular configuration is used, for example, in logistics mission - the wingtips are detached, and the drone looses its capability of horizontal flight in order to simplify controls while the center of mass is moved backwards.

4 Mechanical Design

4.1 Propeller Design

A Propeller is the main propulsion device in the proposed UAV concept. An approximate motor power needed in order to drive each of the propeller is $150W$; thrust-estimation techniques were derived directly from the blade kinematics; some drag and power demand estimation techniques were adopted from [10].

In order to ensure UAV's VTOL capabilities, they should provide total thrust exceeding the drone's Maximal Takeoff Weight (MTO). The propeller was mainly derived from [9]; a theoretical calculations also provide a pretty comparable thrust characteristics. The major differences between the proposed propeller design and the one described in [9] are:

- A custom airfoil: several CLF5605-alike experimentally-designed airfoils were simulated and compared, using an Xfoil simulation capabilities for the low-Reynolds airflows. The best one characteristics, namely "LRT-3" were then used in propeller thrust estimation calculations;
- A diameter of the proposed propellers is $0.9m$ whilst $1.2m$ in [9];
- The angular velocity of each of the propellers is $50Hz$, or $3000RPM$, comparing to $40Hz$ or $2400RPM$ in the one proposed in [9];
- The two propellers are counter-rotating, ensuring a propeller reaction momentum and gyroscope precessions mutual compensation;
- A simple mechanism is implemented in order to ensure a constant-speed capability of the main rotors;
- A constant-rotating speed propeller feature is also useful during a horizontal flight stages, when the undisturbed airflow speed rises;
- An estimated maximal thrust provided by two propellers is approximately equal to $16.2N$ of thrust, or $4.34kg$ of martian weight; this however couldn't be compared with [9] due to lack of information (a gross martian weight of Mars Helicopter described in [9] is $1.8kg$); obviously, the MTO range of the proposed UAV lays below of the estimated thrust of $16.2N$.
- No airflow turbulizers are presumed in propeller design.

The main purpose of the proposed constant-speed rotor mechanism is to secure propeller sections from stalling in some particular airflow conditions. This ensures uninterrupted thrust delivery, even in cases of undisturbed airflow velocity taking negative values. This particular feature provides a flight stability and safety, especially during vertical landing phases.

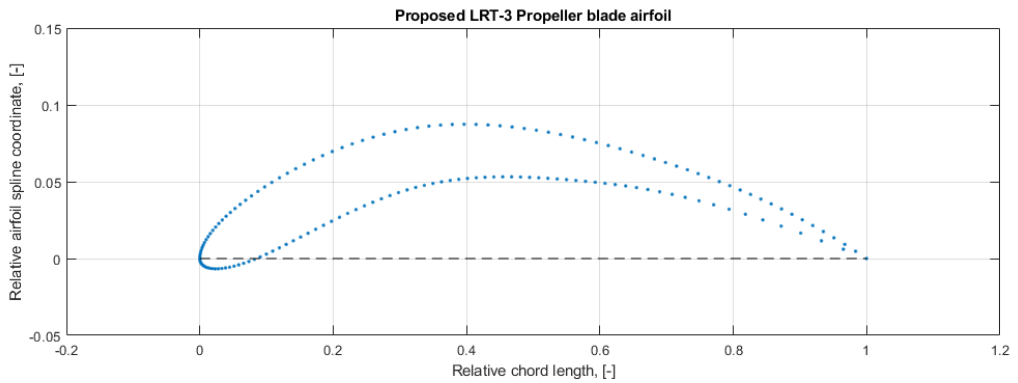


Figure 2: Proposed LRT-3 Propeller blade airfoil coordinates, not to scale.

A chosen propeller blade performance is represented in figure below.

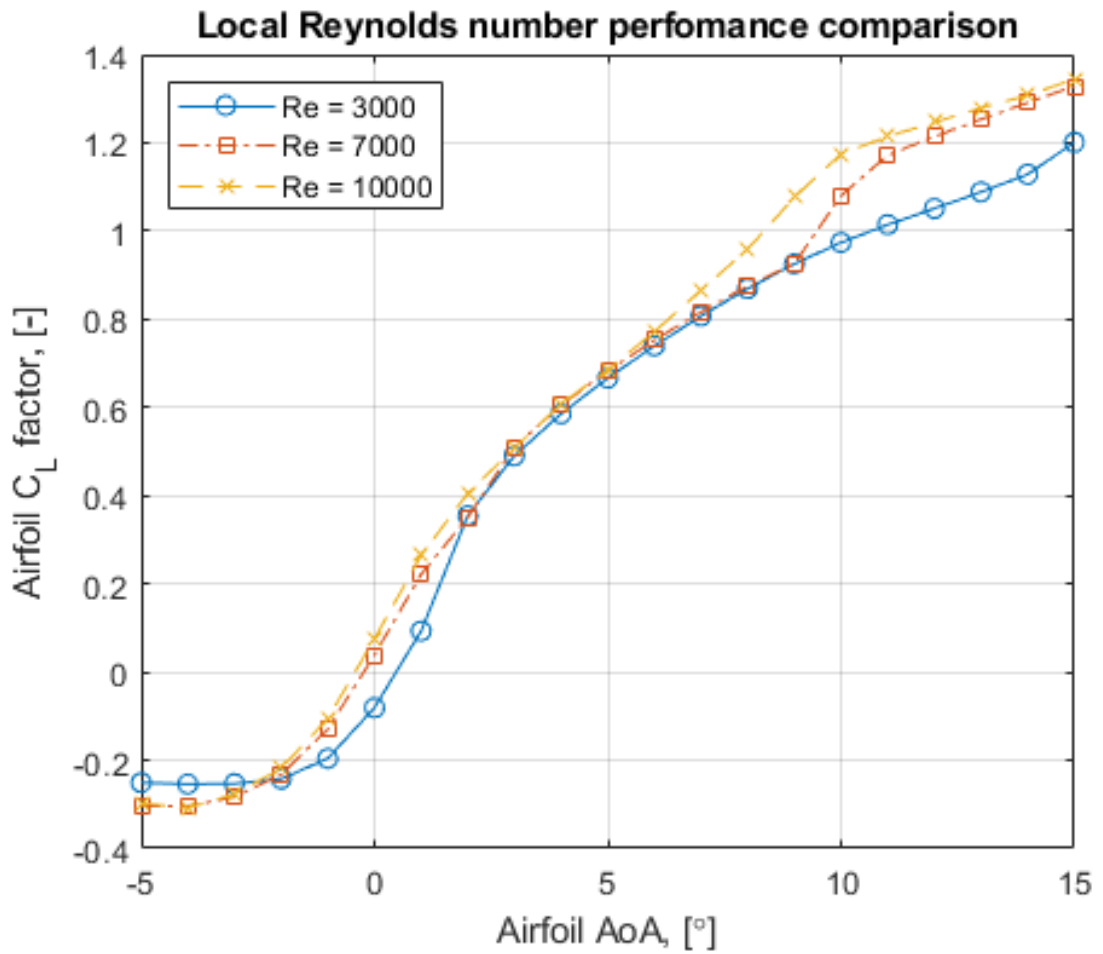


Figure 3: LRT-3 airfoil performance characteristics in function of local Reynolds number

Propeller blade section radius, [m]	0.025	0.125	0.25	0.375	0.45
Local Reynolds number, [Re]	590	4,400	7,100	8,900	5,300
Local Mach number, [-]	0.03	0.17	0.34	0.51	0.61
Blade section thrust contribution	—	4.1%	34.8%	57.5%	3.6%

Table 2: Estimated propeller blade performance per blade sections.

4.2 Wing Airfoil Design

A chosen airfoil for the wing sections is S1223, directly adopted from [11]. This particular airfoil yet introduces a major disadvantage of high aerodynamic momentum. Instead of adding subsequent control surfaces or aerodynamic stabilizers, it is assumed that a control system will be designed in such a way that the present control surfaces will provide lateral stability in each horizontal flight phase.

The estimated flying airspeed of the proposed solution in a given atmospheric conditions varies from 20 to $30 \frac{m}{s}$. The Reynolds numbers range for the given airpseeds varies from 7,000 to 15,000 Re; this range belongs to the unstable flow transitioning from laminar to turbulent. This fact leads to the laminar bubble shift in a wing chord direction; this therefore leads to unpredictability in steering, because of the aerodynamic pitching moment change with the laminar bubble transition.

The solution for the problem described above is in applying a fluid flow turbulizers in order to force laminar bubble transition to a certain chord relative width. The conventional turbulizers applied in earth-like atmospheric conditions are, however, not applicable in martian atmospheric conditions due to extremely low Reynolds numbers range; in order to turbulize the airflow in such a hard environmental conditions, a revolutionary and innovative airflow turbulizing technique is proposed. The applied turbulizers technique is going to be described precisely in section 5.2.

Additionally, a leading-edge slots may be implemented in order to extend the upper AoA range bound, roughly adding additional 3° before airfoil stall.

4.3 Package Picking Mechanism Design

The original concept of the gripper assumed the use of two threaded shafts connected by a friction gear with the gripper jaws mounted on them. A servomechanism was responsible for the drive, which was to set one of the shafts in motion. By means of the implemented gear, the torque was transmitted to a second shaft rotating in the opposite direction to the drive shaft. The clamping process was carried out through the synchronous cooperation of threaded shafts with threaded holes in the base of the gripper's jaws. The process of loosening the grip was carried out in a similar way to clamping, with the difference that the shaft driven by the servomechanism would be rotated in the opposite direction. The stability of the entire structure would be provided by two titanium runners on which the jaws would move while gripping and opening the grip.

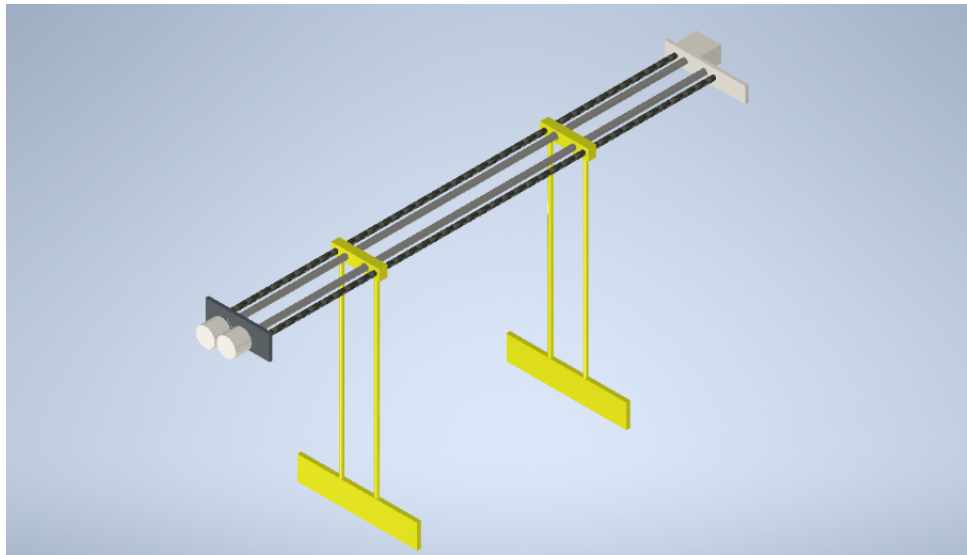


Figure 4: The first concept of a gripper with two drive rods

After analyzing the first prototype, we came to the conclusion that the structure contains many critical points, which is why we decided to simplify it. We resigned from two shafts and a friction gear in favor of one driven shaft with jaws placed on it. In the holes in the bases of the jaws, a left and right thread were used, respectively, to obtain a symmetrical movement of both jaws. Additionally, a third runner has been added for greater rigidity.

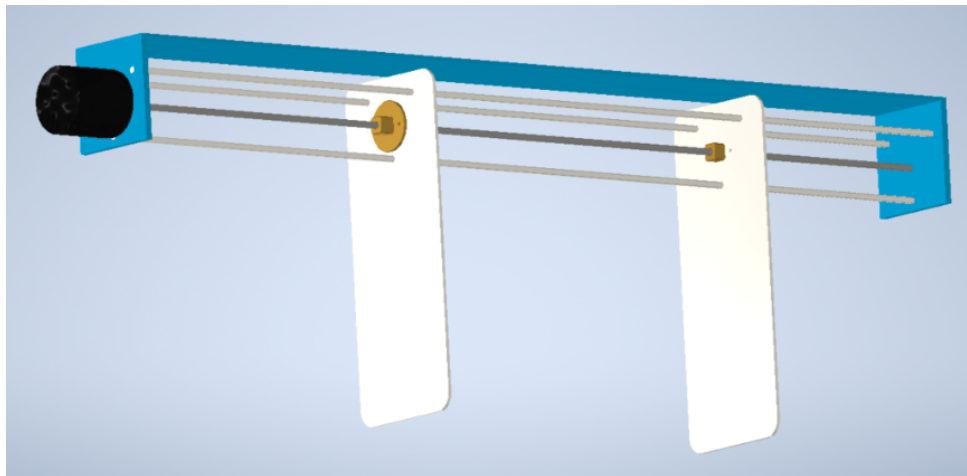


Figure 5: The second concept of a gripper with a single drive rod

After analyzing the previous versions of the gripper, we made a decision to choose the final project. The main factor that we took into account when selecting the structure was the time it took for the gripper to close from the fully open position. In a construction using a threaded rod as a drive, it took too much time. The duration of the gripper closing process is particularly important when lifting the package, because during this time the drone must hover over the package and hold this position until the gripper catches

the package. Another argument in favor of rejecting the previous construction was the presence of dust on Mars. This dust, due to settling in the thread grooves over time, may lead to damage of the thread and immobilization of the mechanism. Attempts to design a sealed housing that could protect the mechanism from dust have shown that such a structure will not find use in our project. The main obstacle was that the structure was too heavy. So we decided on a gripper model that uses a linking rods instead of a threaded rod for the closing and opening mechanism. A great advantage was the significant reduction of the gripper closing time, which final value was $0.3s$. Another advantage was the lack of the need to protect the entire mechanism against Martian dust. It is enough to use ordinary sealants, which are located at the tendon bushings and runners. Most of the parts are made of titanium alloy. The sliding sleeves at the junction of the jaws with the runners and at the joints of the moving elements with the linking rods are made of bronze. The parts of the jaws corresponding to the handle of the package have been covered with high-roughness surfaces, thanks to that we obtained greater friction, which will help in the proper maintenance of the package.

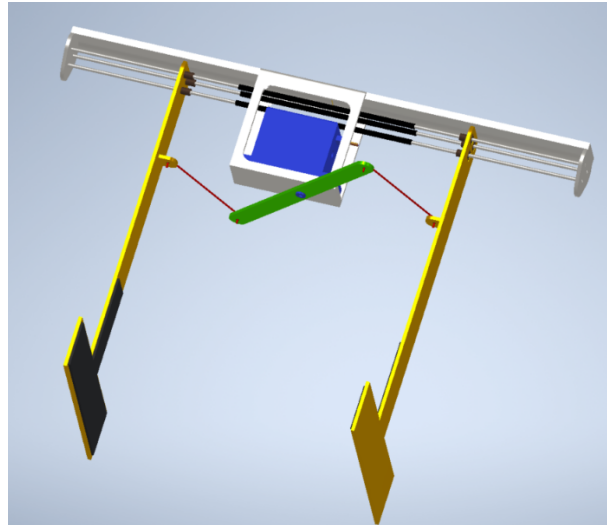


Figure 6: The first projection of the final version of the gripper

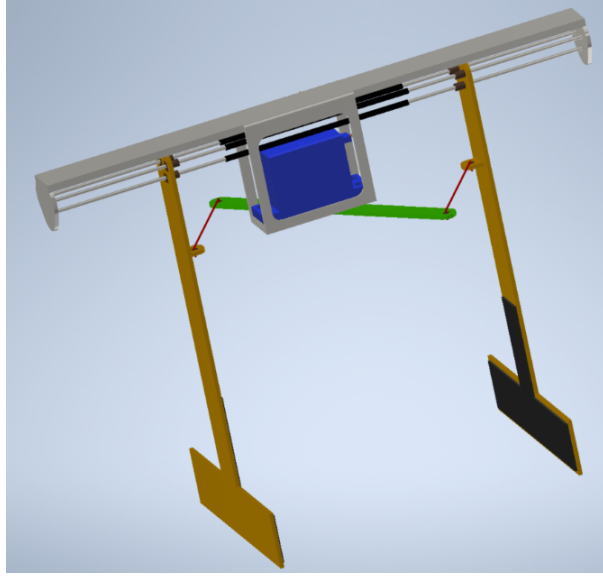


Figure 7: The second projection of the final version of the gripper

We used the *AR-3606HB POLOLU* servo with a maximum torque of $650mNm$ to drive the mechanism. As can be seen from the calculations below, such a moment is sufficient to clamp the gripper with such force that it is possible to lift the package.

Calculations:

$$a_1 = 3.7 \frac{m}{s^2} \text{ -- acceleration due to gravity of Mars}$$

$$a_2 = 2 \frac{m}{s^2} \text{ - take off acceleration of the drone}$$

a - sum of accelerations

G - gravitational force of Mars

$m = 0,1kg$ - package mass

T_1, T_2 - frictional force

N - pressure force

μ - dry friction coefficient

$$\mu = 0.15 - 0.30 \text{ (metal on metal)}$$

For our calculations we take dry friction coefficient titanium on titanium equals to 0.2.

$$a = a_1 + a_2 = 3.7 \frac{m}{s^2} + 2 \frac{m}{s^2} = 5.7 \frac{m}{s^2}$$

$$G = a \cdot m = 5.7 \frac{m}{s^2} \cdot 0.1kg = 0.57N$$

$$T_1 = T_2 = T = \mu \cdot N$$

$$T_1 = \mu \cdot N_1$$

$$T_2 = \mu \cdot N_2$$

$$N_1 = N_2 = N$$

$$G \leq 2 \cdot T$$

$$G - 2 \cdot T = 0$$

$$T = \frac{G}{2} = \frac{0.57N}{2} = 0.285N$$

$$N = \frac{T}{\mu} = \frac{0.285N}{0.2} = 1.425N$$

$$N = F_1 = F_2 = 1.425N$$

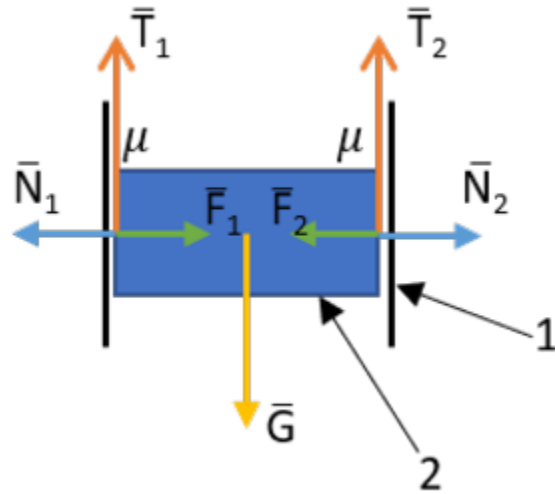


Figure 8: The forces acting on the gripper jaws (1 - gripper jaws; 2 - package)

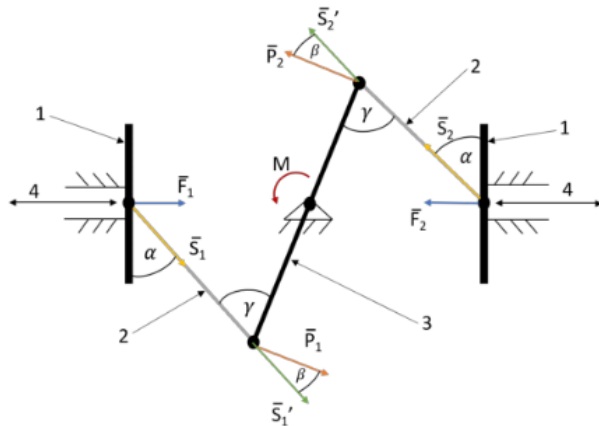


Figure 9: Forces and moments acting on the gripper (1 - gripper jaws; 2 - linking rod; 3 - driving arm; 4 - linear movement)

The following angles' values are given for close position of gripper (package dimensions 15x15x15cm)

Calculations:

$$\alpha = \beta = 27^\circ$$

$$\gamma = 63^\circ$$

$$F_1 = F_2$$

$$S_1 = \frac{F_1}{\sin \alpha} = \frac{1.425N}{\sin 27^\circ} = \frac{1.425}{0.454} = 3.139N$$

$$S'_1 = S_1$$

$$S'_2 = S_2$$

$$P_1 = P_2 = \frac{S_1}{\cos \beta} = \frac{3.139N}{\cos 27^\circ} = \frac{3.139N}{0.891} = 3.523N$$

$$M = 2 \cdot r \cdot P_1 = 2 \cdot 0.07m \cdot 3.523N = 0.494Nm$$

As we know the driving torque and the force that we have to apply to the gripper's jaws, we conducted a strength analysis on the finished model's structure. The results of this analysis were satisfactory. The obtained safety factor at the weakest point was 8.95. The maximum jaw deformation was 1 mm assuming the worst-case scenario, in which the UAV grabs the package with the very end of the jaws, it means the force is applied pointwise on the largest possible arm.

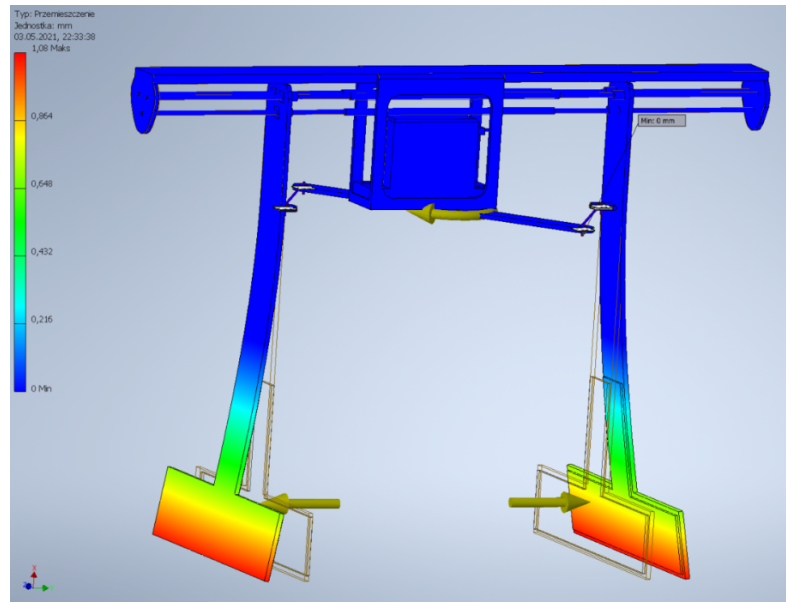


Figure 10: The maximum jaw deformation due to FEM

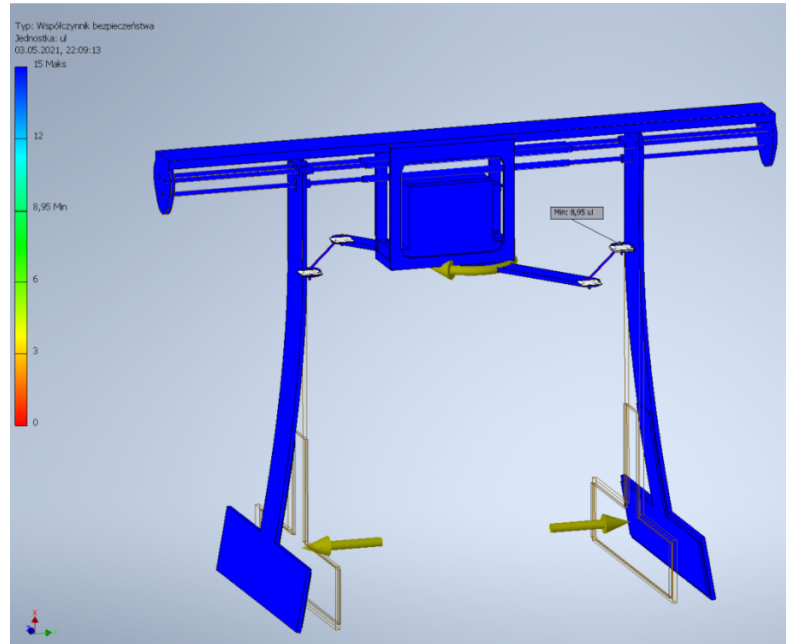


Figure 11: Safety factor due to FEM

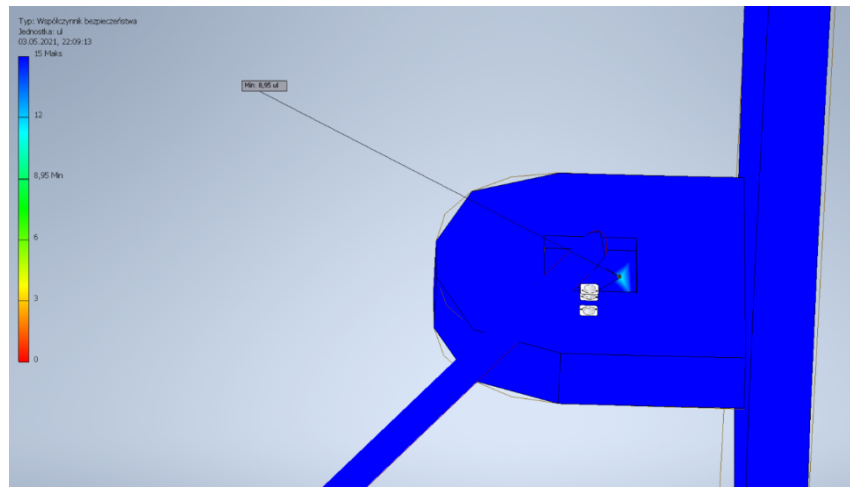


Figure 12: Location of the lowest safety factor

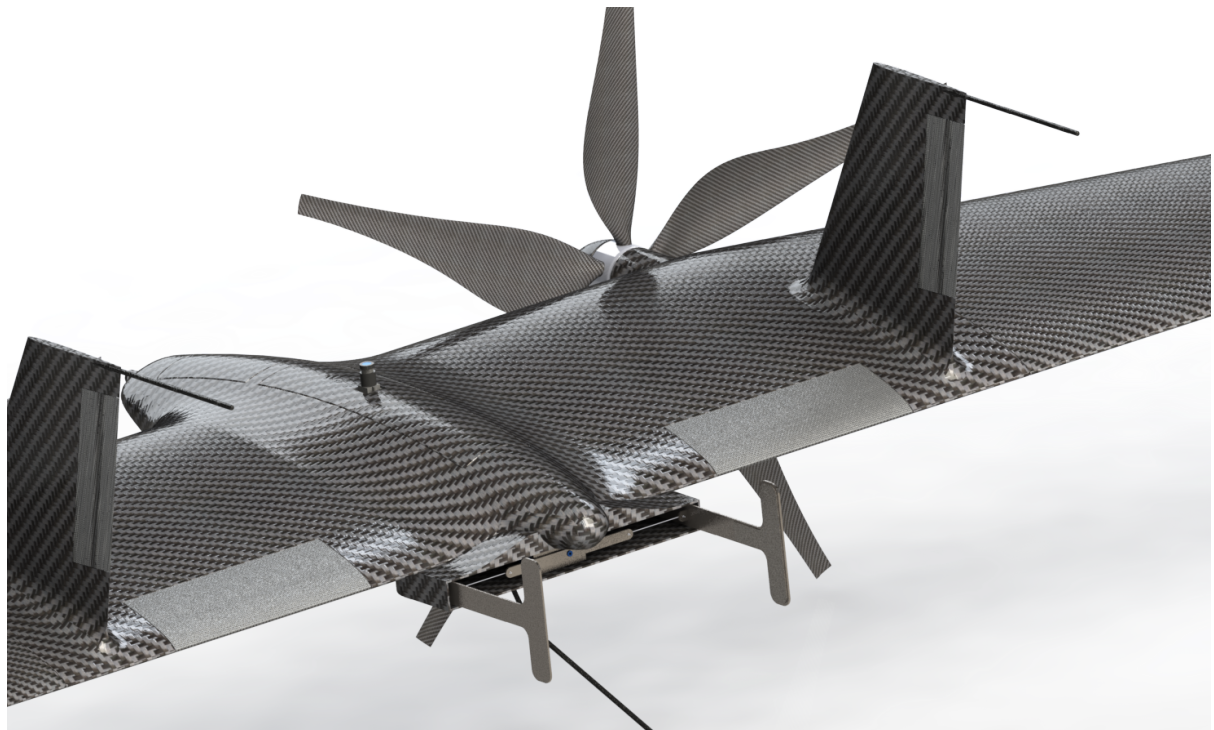


Figure 13: Package Picking Mechanism

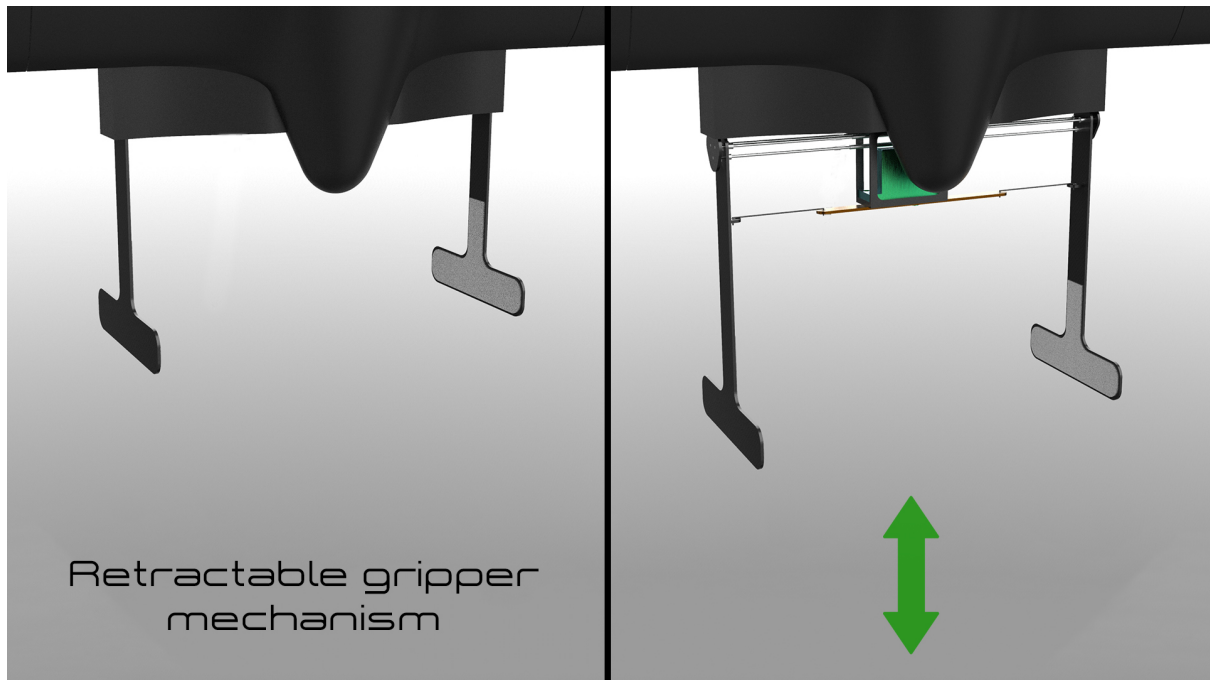


Figure 14: Package Picking Mechanism

5 Electric/Electronics Design

5.1 Electronics System Breakdown Structure

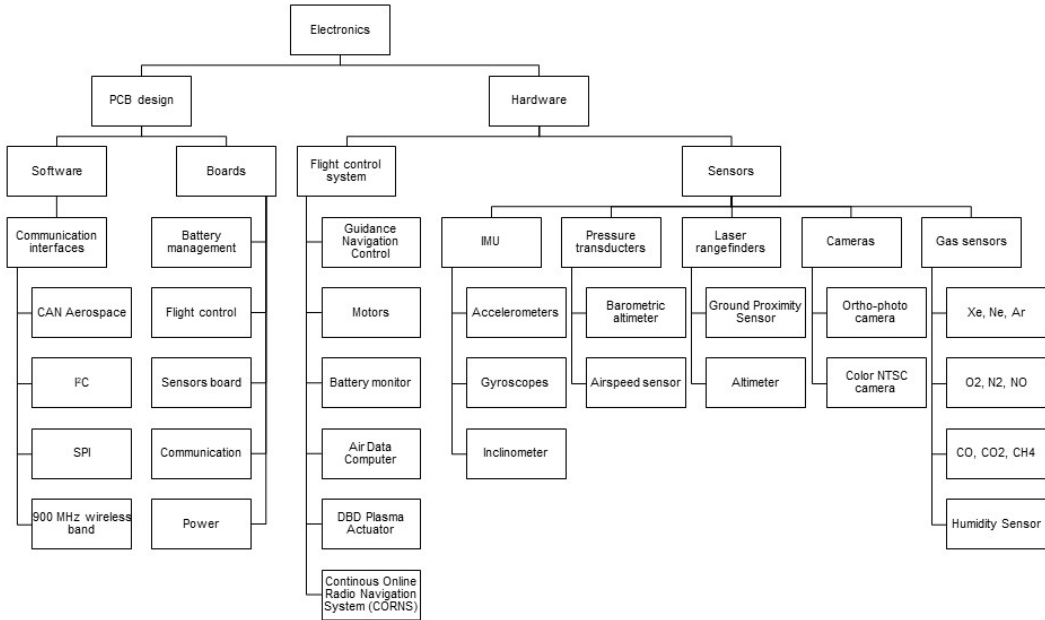


Figure 15: Electronics System Breakdown Structure

Five main PCB boards are used in plane:

- **Battery** — battery interface board is attached to the battery pack and consists the battery monitoring circuit, motor and DBD plasma actuators power switches and current monitor. The battery pack and battery interface board are connected through electrodes to allow battery replacement. Drone is using 8 Sony VTC4 18650 Batteries. Each battery has 2Ah capacity and provide 30A continuous current (52A peak).
- **Flight Control** — this is the heart of the autonomy and all flight controls. NVIDIA Jetson Nano Module with Quad-core ARM Cortex-A57 MPCore processor serves as the low-level flight controller (FC), which includes guidance and navigation control, motors control, battery level monitor and DBD plasma actuators. Such a powerful unit also handles all the sensors data and actuators interface including CORNS system, IMU, pressure transducers, laser rangefinders, cameras and gas sensors.
- **Sensors** — this board is the powerhouse for flight related sensors, cameras and science task sensors. It consists a single core STM32F303 family MCU with an ARM® Cortex®-M4 core and is responsible for collecting data, basic computations and parsing data to FC board.

- **Power** — has two DC/DC converters that regulate the battery voltage to the 3.3 V and the 5 V. It also hosts HV-generator of maximum output voltage 1kVpp for DBD plasma actuators.
- **Communication** — communication module uses COTS 802.15.4 (Zig-Bee) standard 900 MHz chipset. Another STM32F303 MCU is used for monitoring charging current without having to turn on the FC unit, thereby saving power.

Following sensors are used by drone:

- **IMU** — (*Inertial Measurement Unit*) Bosch BMI270 unit combines gyroscopes, accelerometers and inclinometer to measure plane specific forces and angular rates. Signals from IMU are used by AHRS to calculate orientation angles which are used in Flight Control System.
- **Pressure transducers** - measurement of static and total pressure to calculate altitude and airspeed. Bosch BMP390 provides desired accuracy.
- **Laser rangefinders** — Three rangefinders are mounted on drone. TF03 laser range sensor (180 m range) is installed on drone nose as ground proximity sensor. Two auxiliary LIDAR-Lite v3 (40 m range) rangefinders work as altimeters during start and landing operations.
- **CORNS** (Continuous Online Radio-Navigation Subsystem) — another revolutionary and innovative system, proposed by us, dedicated for the navigation purposes. While being pretty similar to existing ILS (Instrument Landing System), this particular subsystem is dedicated for UAV tracking and position estimation. It requires eight narrowband radio channels — two for azimuthal (bearing) localizer, two for inclination localizer, two for full-duplex telemetry and feedback-providing channels, and finally, the rest two for the purposes of two-way phase-shift based rangefinder. A system of four narrow-pattered antennas, located in a presumably known position, mounted on a pan-tilted gimbal are constantly tracking the drone in azimuthal and inclination orientations; in combination with a distance measurement provided by a rangefinder, it is possible to estimate the vehicles position by the means of simple trigonometric calculations.

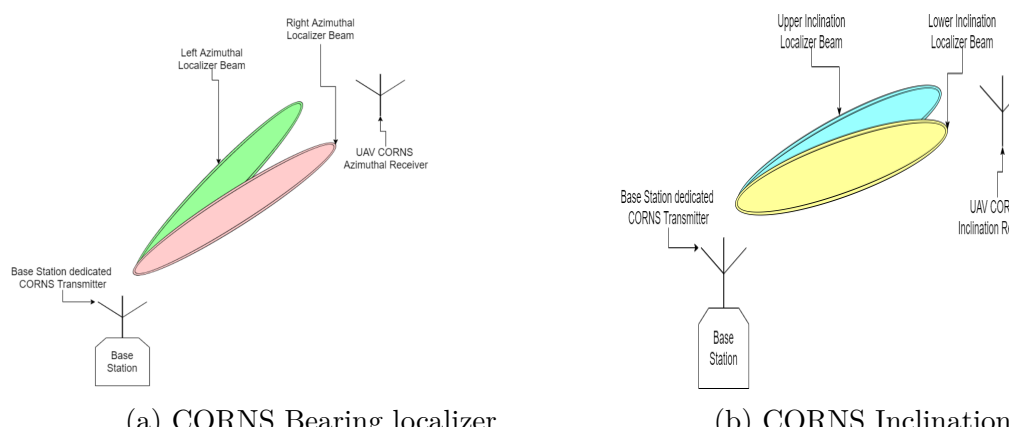


Figure 16: CORNS system.

5.2 Ion Turbulizers

System overview

To ensure sufficient airflow our Team chose to induce some flow with the help of DBD plasma actuators. Proposed design provides active flow control method with its unique advantages including the absence of moving components, fast response, easy implementation, and stable operation. When the actuators are turned on, the stall angle and maximum lift coefficient can be drastically improved. Furthermore the static pressure at the leading edge of the wing can be reduced effectively (in a proper range of angle of attack), which shows the ability of DBD plasma actuators to act as plasma slats. The rolling moment produced by left-side actuation is greater than that produced by the maximum deflection of ailerons, which indicates the potential to also act as plasma ailerons[12] Our team proposes testing of using plasma slats and ailerons on Mars as an additional task as it can simplify future designs even further.

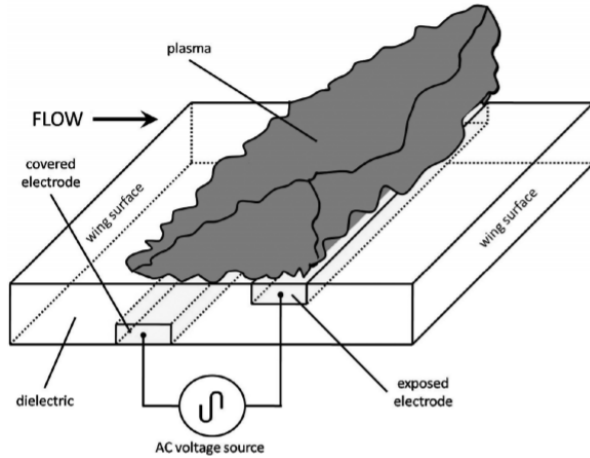


Figure 17: Schematic representation of plasma actuator [13]

The conventional plasma actuator is composed of a pair of electrodes separated by a dielectric layer. When an alternating voltage is applied to the electrodes, a periodic breakdown occurs at the edge of the exposed electrode. During each breakdown event, the charge is transferred from the exposed electrode onto the dielectric surface till the electric field near the electrode drops below the value required for the ionization process. After plasma decay, a volumetric charge is left in the region adjacent to the electrode. This ions are accelerated by the electric field and finally transfer their momentum to the gas [14].

Implementation on Mars Surface.

There are many unknowns related to actuator performance in the reduced air density and high carbon dioxide concentrations of the atmosphere of Mars. For this design, measurements of DBD actuator performance previously made in Earth atmospheric conditions are adapted through trends and constants to estimate performance on Mars. To create the plasma, the voltage applied between the electrodes must be above the breakdown potential of the ambient environment. The breakdown potential relates to the ambient gas composition, and both the pressure and distance between the applied potential bound-

aries, combined into a single term known as the pressure-distance (*pd*) Paschen curves relate the breakdown voltage to the *pd* [15].

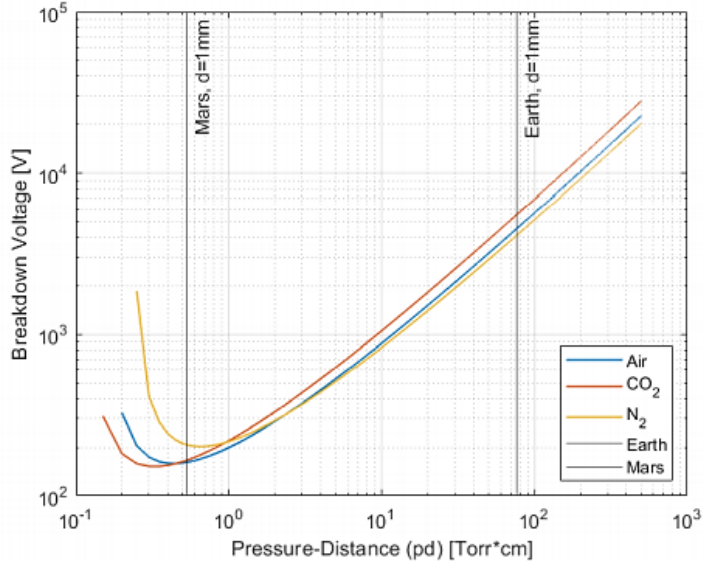


Figure 18: Paschen curves for air, CO_2 and N_2 [15]

The operational point for a DBD plasma actuator with 1 mm electrode separation in 1 atm air is shown in Figure 18 as a vertical line marked ‘Earth’. The operational *pd* 76 Torr-cm at which point the breakdown voltage is 4500V. Actuator operation at 8-25 kV as used in prior works [12, 14, 16, 17]. The equivalent operational point on Mars where ambient pressure is 700 Pa (5.3 Torr) is shown in Figure 18 as a vertical line marked ‘Mars’. The operational *pd* Mars is 0.53 Torr-cm corresponding to a breakdown voltage at 200V. Assuming the same saturation, the operational voltage on Mars will be approximately 0.4-1 kV. This decrease in operational voltage is commensurate with observations [15, 16, 17]. Interestingly it was found that the pulsed mode of operation was far superior to that of continuous actuation and DBD plasma actuators show remarkable performance with reduced duty cycles even at low Reynolds numbers shown on Figure 19a [13, 18, 19, 20]. Duty cycle is the ratio $t_d/t_p \cdot 100$, expressed as a percentage, where, t_d is the portion of the fundamental period t_p over which the device is active. It was also observed that the optimum lies somewhere between 3% and 8% of the duty cycle at low Reynolds numbers (not shown). Moreover, this result is even more significant when we account for the fact that duty cycle percentage correlates linearly with power consumption [20]. The optimal F^+ (reduced burst frequency) discovered previous works [18, 19, 20] lays around at $0.4 < F^+ < 0.6$ with a sharp drop in lift at higher F^+ and therefore modulation frequency needs to be accordingly adjusted to following equation:

$$F^+ = F_\beta c/U_\infty$$

$F_\beta = 1/T_{signal}[\text{Hz}]$ - burst frequency, $U_\infty[\text{m/s}]$ - free stream, $c[m]$ - chord length

As for low pressure and velocity induction in different gasses, numerous studies have shown, that DBD plasma actuators in CO_2 at 1kPa induced velocity at same performance level as they did in air at 1 atm. In the case of CO_2 , the flow velocity essentially increases

as pressure decreases. The plasma actuator could induce the flow in CO₂ at 1kPa which is similar to the condition of Mars atmosphere [21, 22].

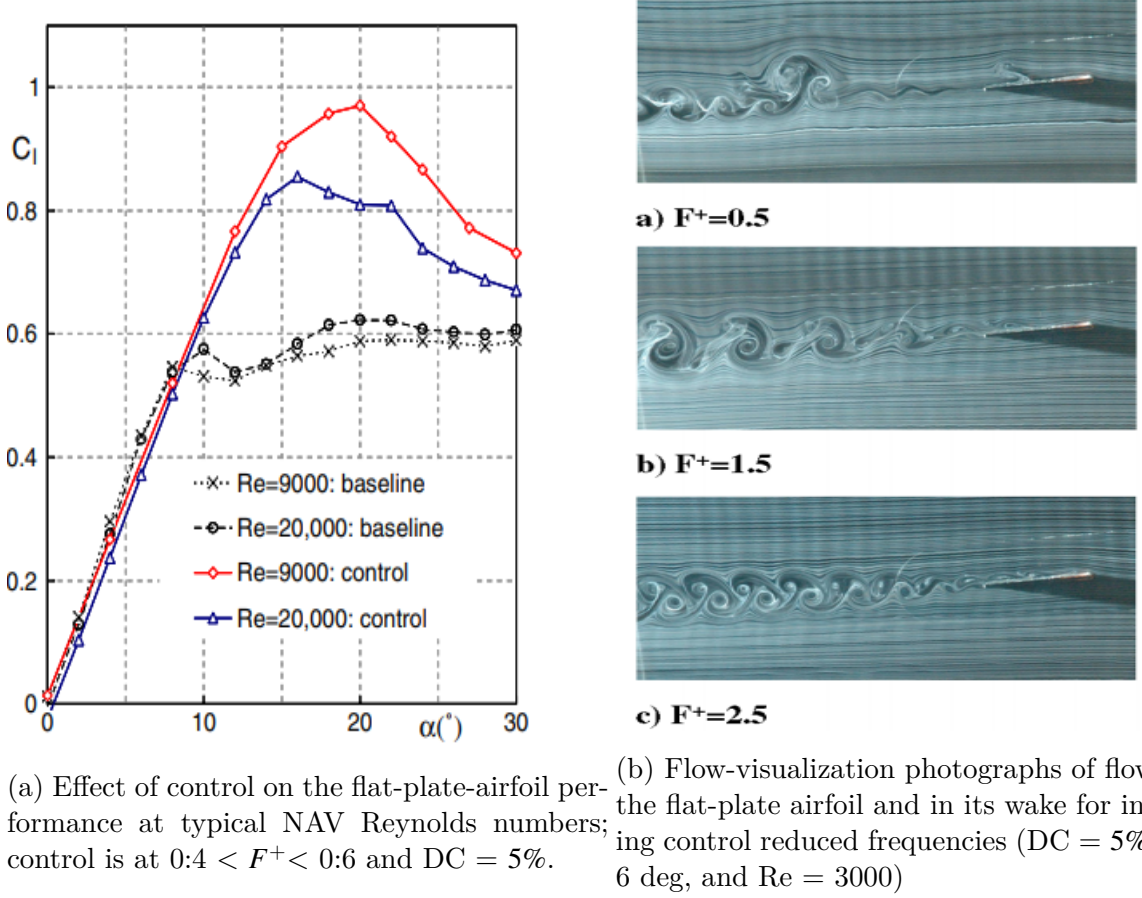


Figure 19: Performance at low Reynolds numbers with optimal settings [19].

Final DBD plasma actuator design

The low weight could be achieved by a precise tuning of the oscillation circuit to the actuator type and length to minimize the reactive power and by limiting the operation to 20% duty cycle. Although the optimal duty cycle is lower (3-8%), due to non linear \$Cl\$ versus \$\alpha\$ curve under some conditions [19] our Team chose to allow more frequent cycles (20%) to ensure absolute best performance. The LiPo battery is used as power supply for the HV-generator. The HV-generator is adjusted to produce a rectangular modulated sine wave of maximum output voltage 1kVpp, adjustable operating frequency (1 to 10 kHz), adjustable modulation frequency (1 to 200 Hz) and adjustable duty cycle (0 to 20%). The placement of the DBD plasma actuator is in parallel arrays. Actuators have linear geometry, as they can perform equally well to their serpentine counterparts [13, 23]. Placing the parallel actuator arrays with little to no separation between each actuator creates destructive interference between the electric field of individual actuators [24, 25]. Larger separations over the induced velocity peak at the downstream edge of encapsulated electrode have been shown to minimize this effect with the effect being essentially the sum of the individual actuators [24, 26]. Chord length of 0.5m allows us to effectively install two actuators in parallel with a length of 1m on each side (while total wingspan is 3m). Mounting actuators on each wing was also the most common in previous works [12, 18]. Furthermore it's a more convenient setup for plasma ailerons

testing. The design implements new multi electrode design in MEE5-SDBD actuator configuration, with highest induced velocity achieved was 91.2% greater than the baseline case while using only 26.2% more power, at the same input voltage [25, 27]. Mounting such a powerful system is intended to support all flight stages, extensively test DBD plasma actuators performance in Mars atmosphere and test alternative functions such as plasma slats, plasma ailerons. All in all, the actuators will use 0.5W/m in default mode, resulting in 2W total. Of course power usage can be cut in half by switching off the second array. We estimate, that at $Re = 15000$, plasma actuation relaxes the stall regime (by around 10°) and increases lift by a maximum of 100% for $\alpha = 10^\circ$ for our airfoil.

5.3 UAV Photogrammetry

Equipment

The UAV will have a fault-free SONY RX100 V camera. It is an example of a camera that can be placed on a UAV, the main factors that should be taken into account when choosing a camera for such a mission are the resolution, size of the sensor (matrix) and weight. The matrix of the selected camera has 20.1 megapixels and a size of 13.2 x 8.8 mm. The estimated weight of the camera without the monitor, viewfinder, battery is about 250 g. The approximate camera weight is 100g.

In the process of camera calibration, we determine the camera constant, coordinates of the main point, and the distortion polynomial coefficients. Camera calibration is performed on a test field (flat or spatial)[28].

An orthomap is a vertical image on which we can take measurements due to the fact that it has a scale. Thus, it differs from ordinary aerial photography. It is obtained from aerial photographs that have distortions due to vehicle movement, distortion of the lens, image perspective and terrain[29].

Along with the photo, the following parameters are being saved: position, height (X, Y, Z) of the UAV at the time of taking the photo, external orientation of the camera (EO) and internal orientation (IO) (focal length (camera constant), coordinates of the main point in the image system and size matrix pixel and distortion). These data will be entered into the computer program together with the photo, using them will improve and speed up the process of creating the photo[30].

In order to create a reliable scale of the map, the actual location of characteristic points on Mars that were on the photomap should be determined. Thanks to such treatments, we can make distance measurements on the resulting product.

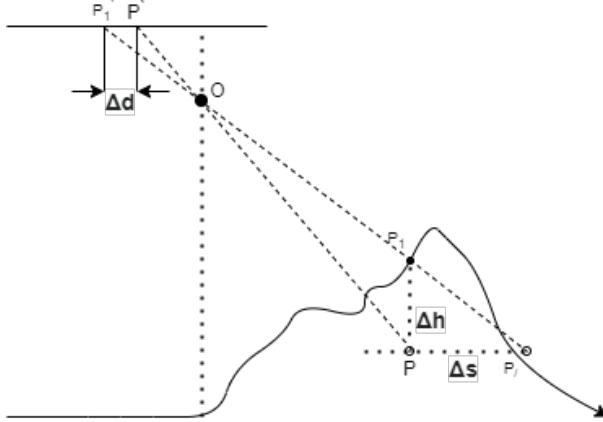


Figure 20: Orthogrammetry data capture concept

5.4 UAV 360° Vision

The UAV will carry an analog vision kit. This solution was chosen for its reliability. Full range receiver with the smallest size among all the receivers in the industry - TBS CROSSFIRENANO RX was chosen. It is a long range FPV receiver with a weight of 0.5g and dimensions of 11 x 18mm. It will use the TBS CROSSFIRE TX long range transmitter based on the latest RF technology. It is capable of self-correcting two-way communication, characterized by low latency and long range. For the set has been selected omnidirectional antenna TBS CROSSFIRE IMMORTAL T V2. It is made of flexible material that allows bending, while minimizing damage that may be caused by collisions. The weight of this antenna is 3.4 g. The antenna contains steel elements that protect it from damage. The equipment will operate at a frequency of 1.2 GHz. Thanks to this it will be possible to fly at long ranges. The GoPro Hero 8 camera will be disassembled and placed in a special housing BETA FPV NakedV2. This is to reduce the weight of the camera from 116 g to 25 g. The device will then be placed in a servo, which will allow 360 degree rotation.

6 Science Package Design

6.1 Science Package System Overview

The system for measuring relative abundance of various gases, relative humidity and temperature consists of a sealed container, a HEPA filter, a sealed closure, a gas and humidity sensor assembly, a temperature sensor and a heater. The container is located at the front of the UAV fuselage and houses all the sensors and the heater. On the inlet to the container there is a HEPA filter in purpose to prevent from entering the dust which can be carried by the wind. A description of how the system works, why the heater should be used and how the test should be conducted is discussed in the Environmental Analysis Process Design subsection.

The sensors used in the container are:

- group of combined AGM sensors (measures Xe , Ne , Ar)
- group of combined AGM sensors (measures O_2 , N_2 , NO)

- OEM gas analyser (measures CO , CO_2 , additionally CH_4)
- used on the Curiosity Rover Vaisala HUMICAP 180RC humidity sensor (full measurement range $0 - 100\%RH$) with integrated $PT - 100$ temperature sensor (measurement range from $-200^\circ C$ to $850^\circ C$) [31, 32, 33, 34]

Each gas sensor has an operating range that allows it to measure the relative abundance of selected gases.

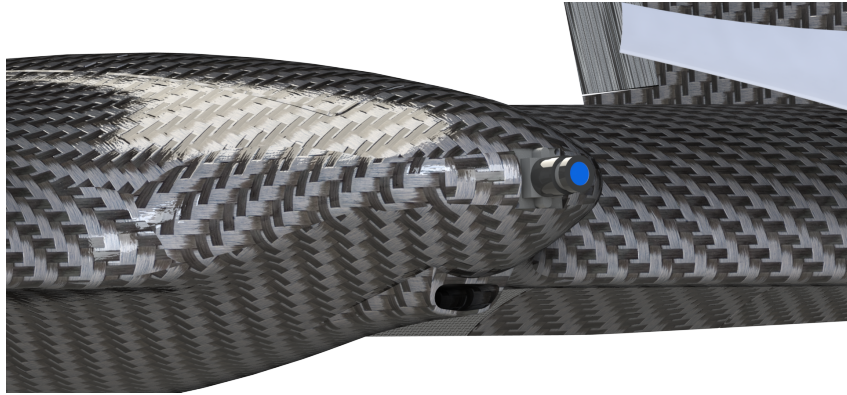


Figure 21: Inlet leading to the container with sensors

6.2 Environmental Analysis Process Design

It is well known from environmental analysis of Mars that temperatures there range from $-153^\circ C$ at the poles to $+30^\circ C$ [5, 6], which for the sensors used exceeds the ability to measure properly at the lowest temperatures. In order to be able to make measurements, a heater was used.

The gas measurement process is as follows. During the flight over the indicated coordinate UAV opens the container and closes it with the collected sample of the atmosphere. If the temperature measured by temperature sensor is above $-70^\circ C$ the measurement of relative abundance of gases is carried out immediately. If the temperature is below $-70^\circ C$, the air in the container is heated until it reaches at least $0^\circ C$. The entire heating process is monitored and the data is recorded. Measurements of the amount of gas due to the constant volume of the container (only the temperature and pressure change) will be the same at each sample temperature, and the measurement itself will be performed correctly due to the sensor range matching the appropriate temperature. Then, knowing the constant volume of the container and the temperature at the point in time, the thermodynamic equations are used to determine the graphs of humidity versus temperature for the range from $-70^\circ C$ to $0^\circ C$. The rest of the graph for temperatures beyond the range of the sensor is approximated with high accuracy using previously collected data and based on the graphs from $-70^\circ C$ to $0^\circ C$ range.

7 UAV Performance Summary

Wingspan, [m]	3.0
Length, [m]	0.75
Height, [m]	0.45
MTO, [kg]	3.5
Estimated minimum flight time in hover, [minutes]	12
Rough optimum flight speed, [$\frac{m}{s}$]	20

Table 3: Proposed solution predicted performance parameters.

List of Figures

1	Isometric Image of the Falcon	1
2	Proposed LRT-3 Propeller blade airfoil coordinates, not to scale.	5
3	LRT-3 airfoil performance characteristics in function of local Reynolds number	5
4	The first concept of a gripper with two drive rods	7
5	The second concept of a gripper with a single drive rod	7
6	The first projection of the final version of the gripper	8
7	The second projection of the final version of the gripper	9
8	The forces acting on the gripper jaws (1 - gripper jaws; 2 - package) . . .	10
9	Forces and moments acting on the gripper (1 - gripper jaws; 2 - linking rod; 3 - driving arm; 4 - linear movement)	10
10	The maximum jaw deformation due to FEM	11
11	Safety factor due to FEM	11
12	Location of the lowest safety factor	12
13	Package Picking Mechanism	12
14	Package Picking Mechanism	13
15	Electronics System Breakdown Structure	14
16	CORNS system.	15
17	Schematic representation of plasma actuator [13]	16
18	Paschen curves for air, CO_2 and N_2 [15]	17
19	Performance at low Reynolds numbers with optimal settings [19].	18
20	Orthogrammetry data capture concept	20
21	Inlet leading to the container with sensors	21

List of Tables

1	Chemical composition of Mars atmosphere in percent or ppm[3]	2
2	Estimated propeller blade performance per blade sections.	6
3	Proposed solution predicted performance parameters.	22

References

- [1] R.E. Novak Y.L. Radeva H.U. Käufli A. Smette A. Tokunaga A. Khayat T. Encrenaz P. Hartogh G.L. Villanueva, M.J. Mumma. A sensitive search for organics (CH_4 , CH_3OH , H_2CO , C_2H_6 , C_2H_2 , C_2H_4), hydroperoxyl (HO_2), nitrogen compounds (N_2O , NH_3 , HCN) and chlorine species (HCl , CH_3Cl) on Mars using ground-based high-resolution infrared spectroscopy. *Icarus*, 223:11–27, 2013.
- [2] Lonnie Shekhtman. With mars methane mystery unsolved, curiosity serves scientists a new one: Oxygen. 2019. <https://www.nasa.gov/feature/goddard/2019/with-mars-methane-mystery-unsolved-curiosity-serves-scientists-a-new-one-oxygen>.
- [3] Dr. David R. Williams. Mars fact sheet. <https://nssdc.gsfc.nasa.gov/planetary/factsheet/marsfact.html>.
- [4] M. Kuhn W. E. Featherstone C. Hirt, S. J. Claessens. Kilometer-resolution gravity field of Mars: MGM2011. *Planetary and Space Science*, 67(1):147–154, 2012.
- [5] <https://mars.nasa.gov/all-about-mars/facts/>.
- [6] <https://web.archive.org/web/20130607140708/http://quest.nasa.gov/aero/planetary/mars.html>.
- [7] National Aeronautics and Space Administration. Mars atmosphere model.
- [8] National Oceanic and Atmospheric Administration. *U.S. Standard Atmosphere*. U.S. Government Printing Office, Washington D.C. 20402, 1976.
- [9] Larry Young Witold Koning Winnie Kuang Carlos Malpica Ames Research Center Moffett Field CA 94035; J. Balaram Theodore Tzanetos Jet Propulsion Laboratory California Institute of Technology Pasadena CA 91109 Shannah Withrow-Maser, Wayne Johnson. Mars science helicopter: Conceptual design of the next generation of mars rotorcraft.
- [10] Preston B. Martin. Rotor blade airfoil design for high-altitude, long-endurance vtol uavs.
- [11] Asif Iqbal Mirza Md Symon Reza, Samsul Arfin Mahmood. Performance analysis and comparison of high lift airfoil for low speed unmanned aerial vehicle. 2016.
- [12] Zhi Su, Jun Li, Hua Liang, Bo-Rui Zheng, Biao Wei, Jie Chen, and Li-Ke Xie. UAV flight test of plasma slats and ailerons with microsecond dielectric barrier discharge. *Chinese Physics B*, 27(10):105205, October 2018.
- [13] Donald P. Rizzetta and Miguel R. Visbal. Numerical investigation of plasma-based control for low-reynolds-number airfoil flows. *AIAA Journal*, 49(2):411–425, February 2011.
- [14] Ivan Moralev, Viktoria Sherbakova, Igor Selivonin, Valentin Bityurin, and Maxim Ustinov. Effect of the discharge constriction in DBD plasma actuator on the laminar boundary layer. *International Journal of Heat and Mass Transfer*, 116:1326–1340, January 2018.
- [15] Juan Rivilla Casado and Amelia D. Greig. Solid state atmosphere breathing plasma propulsion for an autonomous mars drone. In *ASCEND 2020*. American Institute of Aeronautics and Astronautics, November 2020.
- [16] H.L.K. Manning, I.L. ten Kate, S.J. Battel, and P.R. Mahaffy. Electric discharge in the martian atmosphere, paschen curves and implications for future missions. *Advances in Space Research*, 46(10):1334–1340, November 2010.
- [17] Monique M. Hollick, Maziar Arjomandi, and Benjamin S. Cazzolato. An investigation into the sensory application of DBD plasma actuators for pressure measurement. *Sensors and Actuators A: Physical*, 171(2):102–108, November 2011.
- [18] Sven Grundmann, Michael Frey, and Cameron Tropea. Unmanned aerial vehicle (UAV) with plasma actuators for separation control. In *47th AIAA Aerospace Sciences Meeting including The New Horizons Forum and Aerospace Exposition*. American Institute of Aeronautics and Astronautics, January 2009.
- [19] David Greenblatt, Berkant Göksel, Ingo Rechenberg, Chan Yong Schule, Daniel Romann, and Christian O. Paschereit. Dielectric barrier discharge flow control at very low flight reynolds numbers. *AIAA Journal*, 46(6):1528–1541, June 2008.
- [20] B. Göksel, D. Greenblatt, I. Rechenberg, Y. Singh, C. N. Nayeri, and C. O. Paschereit. Pulsed plasma actuators for separation flow control. 2006.
- [21] Masahiko Takagaki, Susumu Isono, Hiroki Nagai, and Keisuke Asai. Evaluation of plasma actuator performance in martian atmosphere for applications to mars airplanes. In *4th Flow Control Conference*. American Institute of Aeronautics and Astronautics, June 2008.

- [22] Takashi Abe, Yuji Takizawa, Shunichi Sato, and Nobara Kimura. A parametric experimental study for momentum transfer by plasma actuator. In *45th AIAA Aerospace Sciences Meeting and Exhibit*. American Institute of Aeronautics and Astronautics, January 2007.
- [23] Mark Riherd and Subrata Roy. Serpentine geometry plasma actuators for flow control. *Journal of Applied Physics*, 114(8):083303, August 2013.
- [24] Flint O. Thomas, Thomas C. Corke, Muhammad Iqbal, Alexey Kozlov, and David Schatzman. Optimization of dielectric barrier discharge plasma actuators for active aerodynamic flow control. *AIAA Journal*, 47(9):2169–2178, September 2009.
- [25] Rasool Erfani, Hossein Zare-Behtash, Craig Hale, and Konstantinos Kontis. Development of DBD plasma actuators: The double encapsulated electrode. *Acta Astronautica*, 109:132–143, April 2015.
- [26] Gabriele Neretti. Active flow control by using plasma actuators. In *Recent Progress in Some Aircraft Technologies*. InTech, September 2016.
- [27] Craig Hale, Rasool Erfani, and Konstantinos Kontis. Multiple encapsulated electrode plasma actuators to influence the induced velocity: Further configurations. In *40th Fluid Dynamics Conference and Exhibit*. American Institute of Aeronautics and Astronautics, June 2010.
- [28] Kraków Jerzy Bernasik. Wykłady z fotogrametrii i teledetekcji. 2008.
- [29] Martinus E. Tjahjadi Silvester S. Sai, “Geometric Accuracy Assessments of OrthophotoProduction from UAV Aerial Images” inThe 1st International Conference on Geodesy Geomatics Catur A. Rokhmana, (2019), and pages 333-344. Land Administration 2019, KnE Engineering.
- [30] <http://colidrone.pl/jak-powstaje-ortofotomapa-i-nmt/>.
- [31] <https://www.vaisala.com/en/press-releases/2012-08/mars-rover-curiosity-equipped-vaisalas-pressure-and-humidity-sensors>.
- [32] <https://www.vaisala.com/sites/default/files/documents/HUMICAP-Sensors-Datasheet-B211748EN.pdf>.
- [33] http://www.sensors-inc.com/Products/Gas_Analysis/Gasmitter.
- [34] http://www.sensors-inc.com/Products/Gas_Analysis/AGM22?fbclid=IwAR3MMb3lwldGsy-ZQ1VHtLBKXqKkg_FFWhhVeRwk7VZsCrodsx3peI6fmc0.